Absolute near-infrared refractometry with a calibrated tilted fiber Bragg grating

Wenjun Zhou,[1,*] David J. Mandia,[2] Seán T. Barry,[2] and Jacques Albert[1]

[1]*Department of Electronics, Carleton University, 1125 Colonel By Drive, Ottawa K1S 5B6, Canada*

[2]*Department of Chemistry, Carleton University, 1125 Colonel By Drive, Ottawa K1S 5B6, Canada*

**Corresponding author: wenjun.zhou@carleton.ca*

Received February 13, 2015; revised March 7, 2015; accepted March 18, 2015;
posted March 18, 2015 (Doc. ID 233698); published April 8, 2015

The absolute refractive indices (RIs) of water and other liquids are determined with an uncertainty of ±0.001 at near-infrared wavelengths by using the tilted fiber Bragg grating (TFBG) cladding mode resonances of a standard single-mode fiber to measure the critical angle for total internal reflection at the interface between the fiber and its surroundings. The necessary condition to obtain absolute RIs (instead of measuring RI changes) is a thorough characterization of the dispersion of the core mode effective index of the TFBG across the full range of its cladding mode resonance spectrum. This technique is shown to be competitive with the best available measurements of the RIs of water and NaCl solutions at wavelengths in the vicinity of 1550 nm.

OCIS codes: (060.3735) Fiber Bragg gratings; (060.2370) Fiber optics sensors; (060.2400) Fiber properties.
http://dx.doi.org/10.1364/OL.40.001713

There have been numerous reports of optical fiber and waveguide-based refractive index (RI) sensors, but in the vast majority of cases, these are used to measure RI changes [1–5]. In such cases, the interferometric devices of the Fabry–Perot or Mach–Zehnder families can provide the best sensitivities, because this parameter scales directly with the path length imbalance, although at the cost of a reduced dynamic range. Absolute refractometry, i.e., the capability to unambiguously determine the RI of a medium by a device with no pre-determined or reference starting point, is quite another challenge. The most widely used refractometer is the Abbe refractometer [6], which is essentially a glass prism with a known, relatively high RI. Substances to be measured can be deposited on the base of this refractometer. A beam of light incident from inside the prism reflects off its base at a plurality of angles and the observation of the reflected light allows the determination of the critical angle, from which the RI of the substance is easily calculated from Snell's law. Another kind of absolute refractometer results from measuring the Fresnel reflection of light at the interface between two media [7]. In this case, extreme care must be taken to reduce the signal noise and to provide an accurate power reference, because the sensitivity of the reflection coefficient to the RI is not very high. While it is possible to deal with all these issues, and indeed, to measure absolute RIs with high resolutions (approaching 10^{-6} in the best commercial refractometers), this requires very elaborate instrumentation and controlled environments. Providing such measurements at different wavelengths further complicates the issue. It is therefore our purpose to show how a relatively simple, easy-to-use miniature fiber refractometer that was first demonstrated in [8] can be calibrated to provide absolute values of the RI at near-infrared (NIR) wavelengths, as compared to the best available data. This fiber-optic absolute refractometer is based on a tilted fiber Bragg grating (TFBG) and an elaborate calibration that allows a direct correspondence to be made between resonance wavelengths and absolute RI. The operation principle of the proposed device is based on the same underlying principle as the Abbe refractometer, i.e., on the determination of the guided leaky-mode boundary, which is made using the effective refractive index (ERI) of the cladding mode closest to that boundary as a measure of the surrounding refractive index (SRI). Verification of the performance of the device is done by immersion in deionized (DI) water and NaCl-water solutions with NaCl mass concentrations from 2% to 26%, corresponding to the validated SRI data from 1.315 to 1.361 at 1550 nm at a normal temperature and atmospheric pressure [6,7,9].

Figure 1(a) illustrates a schematic diagram of the TFBG-based refractometer. It is well known that the TFBG structure can couple the incident core mode into the reflected core mode and a large number of reflected cladding modes [10]. Using a geometrical optics analogy, the excited cladding modes with different ERIs can be represented by propagating plane waves with different incident angles at the cladding-surrounding interface

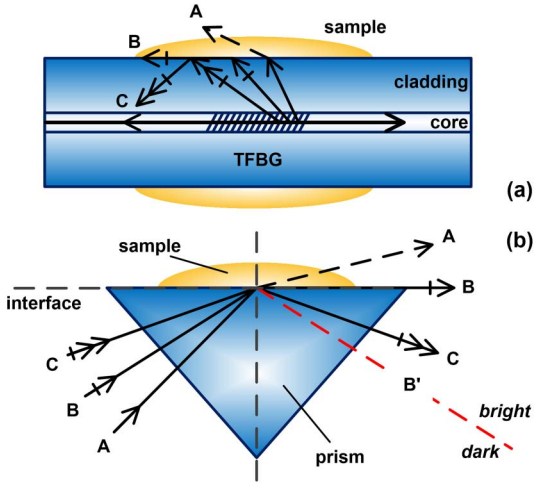

Fig. 1. Schematic diagrams of (a) the TFBG-based refractometer, and (b) the Abbe refractometer. The arrows of A, B, and C represent the propagations of the leaky mode, the cutoff mode, and the guided mode, respectively.

[11]. Leaky cladding modes with ERIs lower than the SRI have incident angles that are smaller than the critical angle for the total internal reflection (mode A in Fig. 1), while the guided cladding modes with a higher ERI than the SRI have incidence angles larger than the critical one (mode C), and are thus totally reflected inside the fiber. The TFBG-based refractometer is thus completely analogous to an Abbe refractometer (as shown in Fig. 1(b)), where the SRI of a sample is determined by measuring the critical angle of the total internal reflection occurring at the sample prism interface (the optical ray labeled B in Fig. 1(b)). If one of the cladding modes of a TFBG has an ERI that is equal to the SRI, it will be regarded as a "cut-off" cladding mode (mode B in Fig. 1(a)) with a corresponding incidence angle equal to that of the critical angle of the equivalent Abbe refractometer. The ERI of this cladding mode (and hence the SRI) can be determined with precision from its resonance wavelength through the grating phase-matching relation. If no cladding mode has an ERI equal to the SRI, then the closest cladding mode ERI value is used, resulting in a maximum error that is less than the spacing between the cladding mode ERIs in this region of the TFBG spectrum. In this respect, it is fortunate that the cladding modes distribution in a 125 μm diameter fiber is very dense, which limits this error, as will be shown below.

The standard phase-matching condition for the resonance wavelengths of the core mode λ_{co} and of any cladding mode λ_{cl} in the TFBG transmission spectrum can be expressed as [10]

$$\lambda_{co} = 2n_{eff}^{co}(\lambda_{co})\Lambda, \tag{1}$$

and

$$\lambda_{cl} = [n_{eff}^{co}(\lambda_{cl}) + n_{eff}^{cl}(\lambda_{cl})]\Lambda, \tag{2}$$

where $n_{eff}^{co}(\lambda_{co})$ and $n_{eff}^{co}(\lambda_{cl})$ are the ERIs of the core mode at the wavelengths of λ_{co} and λ_{cl}, respectively, $n_{eff}^{cl}(\lambda_{cl})$ is the ERI of the cladding mode at λ_{cl}, and Λ is the projection of the actual grating period along the fiber axis due to the tilt angle of grating planes. By substituting Eq. (1) into Eq. (2), the ERI of the TFBG cladding mode can be written independently of Λ as

$$n_{eff}^{cl}(\lambda_{cl}) = \frac{2\lambda_{cl}}{\lambda_{co}} n_{eff}^{co}(\lambda_{co}) - n_{eff}^{co}(\lambda_{cl}). \tag{3}$$

As a result, for any cladding mode resonance in the TFBG spectrum, its ERI can be calculated from its measured wavelength position and that of the core mode, provided that the corresponding ERIs of the core mode at the two resonant wavelengths are also known. While the resonance wavelengths can be measured with an accuracy of 1 part in 10^5, the core mode ERIs as functions of the wavelength are not so well known, mostly because of the fiber fabrication tolerances (doping and geometry), but also because the average RI of the core glass is modified during the UV irradiation used to fabricate the TFBG [10]. It is therefore imperative to calibrate the core index dispersion with the greatest possible precision on a TFBG that is to be used for absolute refractometry. The process to do so is to compare the cladding mode resonance positions of the TFBG in air (i.e., with a precisely known and temperature-independent SRI of 1.000273 [12]) to the simulated values using an exact vector mode calculation, and to adjust the core RI of the simulation until the resonance positions match across the whole spectrum.

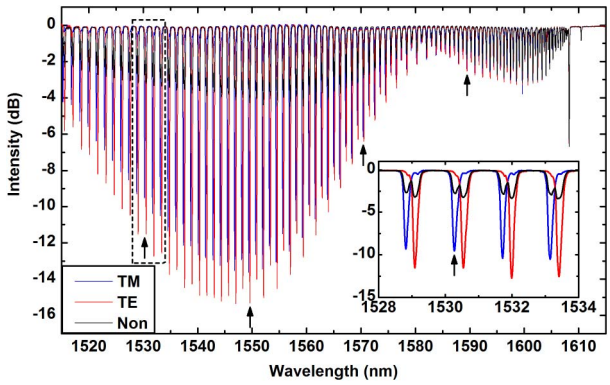

Fig. 2. TFBG spectra measured under TM-, TE-, and nonpolarized lights. The black arrows mark the wavelength positions of the four polarized cladding modes selected for the simulations.

Figure 2 shows the transmission spectra of a 10° TFBG written in a hydrogen-loaded CORNING single- mode fiber (SMF-28) with a pulsed KrF excimer laser using a phase mask with a period of 1112.03 nm. Here, we propose a new method to calculate the wavelength-dependent ERI of the core mode (chromatic dispersion) of a TFBG from the measured spectra and vector mode simulations. First, the ERIs of the core mode are calculated at several resonance wavelengths found in the TFBG transmission spectrum (as shown in Fig. 2), i.e., the Bragg reflection of the core mode upon itself (1610.49 nm) and four polarized cladding modes (1530.27, 1549.62, 1570.40, and 1589.52 nm), using a vectorial mode fiber solver (the GFS solver in FIMMWAVE, by Photon Design). In the simulation model, the geometric structure of the SMF waveguide includes a core layer with a diameter of $8.3(\pm \sim 0.07)$ μm, a cladding layer with a diameter of $125.0(\pm 1.0)$ μm, and a surrounding air layer with a thickness of 17.5 μm. The dispersion-corrected default values of the RIs of the core and cladding glass are those from [13], with a nominal GeO_2 fraction of 0.0425 in the GeO_2–SiO_2 system of the SMF core material. This initial simulation does not provide a good fit to the measured ERIs because of the increased UV-induced average RI in the TFBG [14,15]. In order to reproduce the measured data, the core RI used in the simulation is then artificially modified by changing the equivalent fraction of GeO_2 and recalculating the RI dispersion of the core glass by the relationship given in [13]:

$$n_{fiber}(\lambda) = \sqrt{1 + \sum_{i=1}^{3} \frac{[A_i + f(C_i - A_i)]\lambda^2}{\lambda^2 - [B_i + f(D_i - B_i)]^2}}. \tag{4}$$

Here, A_i, B_i, C_i, and D_i are the Sellmeier coefficients for the SiO_2 and GeO_2 materials, respectively, shown in

Table 1. Sellmeier Coefficients for Eq. (4)

i	1	2	3
A_i	0.6961663	0.4079426	0.8974794
B_i	0.0684043	0.1162414	9.896161
C_i	0.80686642	0.71815848	0.85416831
D_i	0.068972606	0.15396605	11.841931

Table 1, f is the fraction of GeO_2, and λ is the wavelength (in units of μm). For the case of $f = 0$, Eq. (4) describes the RI dispersion of the pure silica material for the SMF cladding layer. The RI of the air layer is set at 1.00027. Thus, the ERIs of the core mode at the five selected wavelengths are simulated for the GeO_2 fractions in the range from 0.04 to 0.06. As shown in Fig. 3(a), the ERIs of the core mode increase linearly with the GeO_2 fraction at a fitted slope of 0.12476 averaged over the five wavelengths. Secondly, the corresponding ERIs of four polarized cladding modes (at 1530.27, 1549.62, 1570.40, and 1589.52 nm) can be calculated with Eq. (3), based on the measured resonance wavelengths and the simulated results of the core mode indices in Fig. 3(a), as functions of the GeO_2 fraction, resulting in the open symbols in Fig. 3(b). Finally, the four individual vectorial modes ($TM_{0,51}$, $TE_{0,44}$, $TM_{0,35}$, and $HE_{1,25}$) with ERIs closest to those obtained in the second step were simulated, also as functions of the GeO_2 fraction. Here, a polarized TFBG spectrum is used to maximize the accuracy of the resonance positions, given that the cladding in air is not weakly guiding and that polarization splitting of the modes is observed in Fig. 2 [14–16]. The simulated results are indicated by solid symbols in Fig. 3(b). This clearly shows that there is a value of the GeO_2 fraction that provides the best fit between the measured and simulated cladding mode ERIs. This value (the average of the four crossing points in Fig. 3(b)) is 0.0523, and the largest deviation of 0.0011 occurs for the "1530 nm" mode.

An equivalent GeO_2 fraction of 0.0523 can then be used to calculate the core RI dispersion for this TFBG by Eq. (4). The simulated ERI of the core mode at the Bragg wavelength of 1610.49 nm is 1.44753 ($\pm 1.3 \times 10^{-4}$) (using the maximum GeO_2 fraction deviation of 0.0011 to estimate the ERI uncertainty). Since the resonance wavelengths of the TFBGs can be measured with a precision of 1 in 10^5, the ERIs of all of the measured cladding modes can be calculated from their wavelengths by Eq. (3), with a maximum uncertainty also of the order of 10^{-4}. Following the calibration as above, the TFBG refractometric accuracy is validated by the measurements in saline (NaCl) solutions with a mass concentration from 0% (DI water) to 26% (saturated) at a temperature of 22(±1)°C, and by a comparison to the literature values. The TFBG was held straight on a fiber holder, and within 0.5 mm of the surface of a microscope slide. The saline solutions with various concentrations were dispensed with pipettes onto the slides and covered the TFBG area completely. The TFBG and slides were cleaned by DI water and dried in air thoroughly between each measurement. A broadband source (JDSU BBS1560) and an optical spectrum analyzer (ANDO AQ6317B) were used for the measurements.

Since the modes of interest (weakly guided near the cutoff and leaky) no longer have polarization splitting [14,17], all of the TFBG spectra were measured using nonpolarized light. The measured spectra for various concentrations of the saline solutions are shown in Fig. 4, where the cutoff cladding mode resonance for each concentration is indicated. The cutoff mode is

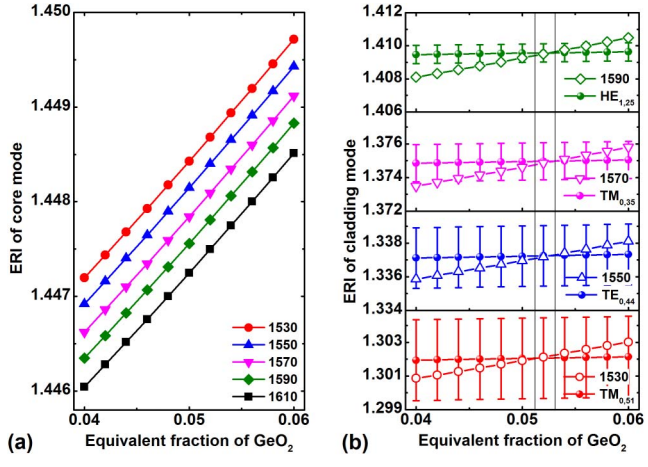

Fig. 3. ERIs of (a) the core modes, and (b) the cladding modes at different wavelengths versus the equivalent fraction of GeO_2 (see text for details). The error bars indicate the simulated ERIs' uncertainties of the polarized cladding modes caused by the geometrical uncertainties of the SMF waveguide. No absolute error bars of the core mode indices are plotted, due to the maximum magnitude of 4×10^{-5}.

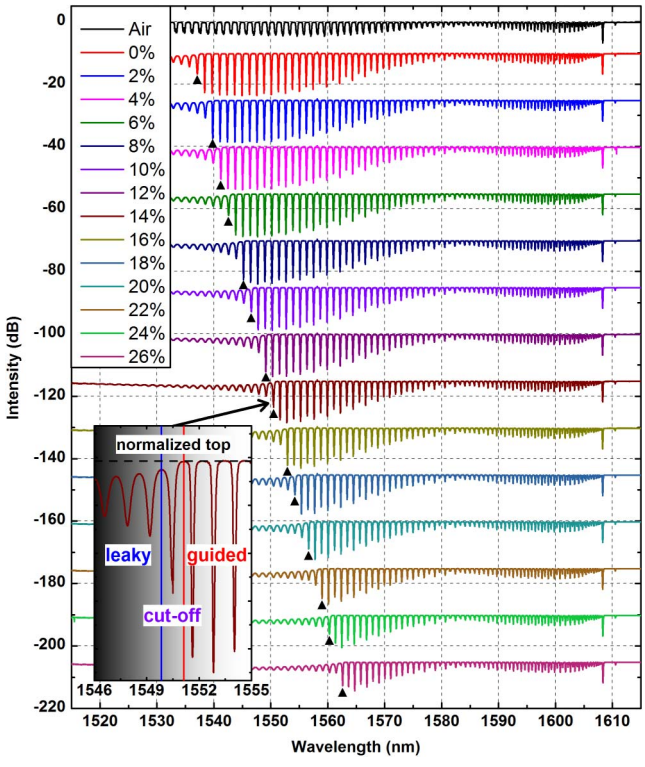

Fig. 4. Nonpolarized TFBG spectra measured under the surroundings of air and saline solutions with various mass concentrations (spectra offset by 15 dB for clarity). The corresponding position of the cutoff cladding mode for each concentration is marked with a black triangle. Inset: detailed spectrum of the cutoff mode resonance for the concentration of 14%.

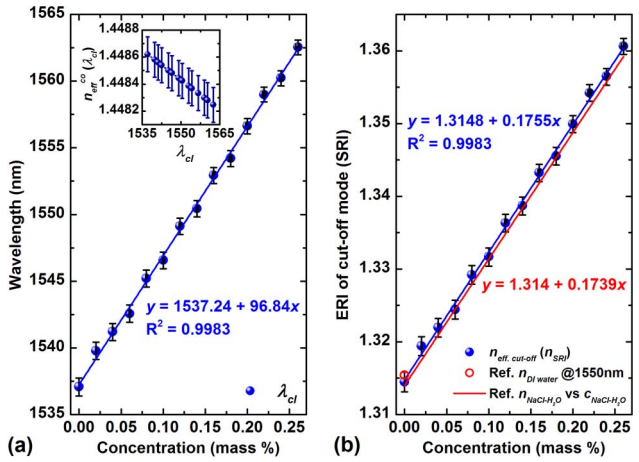

Fig. 5. (a) Wavelengths of the cutoff mode resonances versus the mass concentrations of the saline solutions. Inset: simulated ERI of the core mode at each cutoff wavelength. (b) Calculated ERIs of the cutoff cladding modes (i.e., SRI) with comparative data from [6,7].

identified, as shown in the inset of Fig. 4, by the first resonance (going toward short wavelengths) for which the out-of-resonance transmission (i.e., the transmission maxima on each side of the transmission dip) decreases below the baseline determined by the top level of the remainder of the spectrum on the long wavelength side. Figure 5(a) shows the extracted wavelengths of the cutoff mode resonances from the TFBG spectra shown in Fig. 4.

As always in high-accuracy TFBG spectral measurements, in order to compensate for the potential temperature difference between the measurements, the spectra are all shifted to make their Bragg wavelengths coincide. Therefore, the corresponding vertical error bars do not reflect the measurement uncertainty (below 0.01 nm in this case), but rather indicate half the wavelength separations between the cutoff mode resonance and the adjacent resonances (because it is known with certainty that one of these is guided and the other leaky). For these cutoff mode wavelengths, the ERIs of the core mode were simulated with the calibrated GFS fiber solver and shown in the inset of Fig. 5(a). Finally, Eq. (3) was used to calculate the ERIs of the cutoff cladding modes (which are equal to the SRI, within the uncertainty mentioned above). The calculated ERIs versus the mass concentrations are shown in Fig. 5(b). The linear fitting line in Fig. 5(b) shows that the calibrated RI of the saline solution at 1550 nm increases with the mass concentration in weight percentage with a slope of 0.1755. The literature values are also reported on the graph for comparison. In particular, the slope of a similar measurement obtained using the power-referenced Fresnel reflection at the tip of a fiber was found to be 0.1739 (a difference of less than 1%), with a value at a zero NaCl concentration of 1.314 [7]. Here, the corresponding result is 1.3148 (±0.0013), while the well-accepted value for the RI of the DI water at 1550 nm measured by an Abbe refractometer is 1.3154 (±0.0004) at 20°C [6]. Since the major source of uncertainty in our measurement results from the spacing of the resonances, this could be improved by using a larger, nonstandard fiber cladding diameter, where the mode density would be higher.

In conclusion, we proposed a TFBG-based Abbe refractometer for absolute RI measurements (lower than 1.4) at wavelengths near 1550 nm. It is the calibration of the TFBG and its resonances in the known RI of air that allows for the correlation of the cutoff positions of the cladding mode with the absolute RI of other media in which the TFBG is immersed. No temperature control is needed for the TFBG (keeping in mind that the RI to be measured is itself temperature-dependent), and the RI uncertainty is about $\pm 10^{-3}$. This value is relatively high, but remains of practical use for absolute measurements, especially since only large, temperature-compensated and expensive bench top Abbe refractometers can provide better resolution (10^{-4}) at these wavelengths. Note that the TFBGs can measure refractive index changes with a much better accuracy of 10^{-5} [10].

This work was supported by the Natural Sciences and Engineering Research Council of Canada, the Canada Foundation for Innovation, and the Canada Research Chairs program.

References

1. S. Pevec and D. Donlagic, Opt. Lett. **39**, 6221 (2014).
2. L. Mosquera, D. Sáez-Rodriguez, J. L. Cruz, and M. V. Andrés, Opt. Lett. **35**, 613 (2010).
3. W. Zhou, X. Dong, L.-Y. Shao, C. C. Chan, C.-L. Zhao, and P. Shum, Sens. Actuators A **168**, 46 (2011).
4. Y. Ma, X. Qiao, T. Guo, R. Wang, J. Zhang, Y. Weng, Q. Rong, M. Hu, and Z. Feng, Opt. Lett. **37**, 323 (2012).
5. J. Wo, G. Wang, Y. Cui, Q. Sun, R. Liang, P. P. Shum, and D. Liu, Opt. Lett. **37**, 67 (2012).
6. S. Kedenburg, M. Vieweg, T. Gissibl, and H. Giessen, Opt. Mater. Express **2**, 1588 (2012).
7. Y. T. Wu, X. G. Huang, and H. Su, Appl. Phys. Lett. **91**, 131101 (2007).
8. G. Laffont and P. Ferdinand, Meas. Sci. Technol. **12**, 765 (2001).
9. P. Schiebener, J. Straub, J. M. H. Levelt Sengers, and J. S. Gallagher, J. Phys. Chem. Ref. Data **19**, 677 (1990).
10. J. Albert, L.-Y. Shao, and C. Caucheteur, Laser Photon. Rev. **7**, 83 (2013).
11. A. Yariv and P. Yeh, *Photonics: Optical Electronics in Modern Communications* (Oxford University, 2007).
12. P. E. Ciddor, Appl. Opt. **35**, 1566 (1996).
13. J. W. Fleming, Appl. Opt. **23**, 4486 (1984).
14. W. Zhou, D. J. Mandia, S. T. Barry, and J. Albert, Opt. Express **22**, 31665 (2014).
15. W. Zhou, D. J. Mandia, M. B. E. Griffiths, S. T. Barry, and J. Albert, J. Phys. Chem. C **118**, 670 (2014).
16. M. Z. Alam and J. Albert, J. Lightwave Technol. **31**, 3167 (2013).
17. Y.-C. Lu, R. Geng, C. Wang, F. Zhang, C. Liu, T. Ning, and S. Jian, J. Lightwave Technol. **28**, 1677 (2010).